Proper Generalized Decomposition stereocorrelation to measure kinematic fields for high speed impact on laminated glass

Xuyang Chang, Corentin Le Gourriérec, François Hild, Léonard Turpin, Myriam Berny, Stéphane Roux

Proper Generalized Decomposition Stereocorrelation to Measure Kinematic Fields for High Speed Impact on Laminated Glass

Xuyang Chang[a,*], Corentin Le Gourriérec[a,b], Léonard Turpin[a,1], Myriam Berny[a], François Hild[a], Stéphane Roux[a]

[a] *Université Paris-Saclay, CentraleSupélec, ENS Paris-Saclay, CNRS LMPS–Laboratoire de Mécanique Paris-Saclay, 4 Avenue des Sciences, 91191 Gif-sur-Yvette, France*
[b] *Saint-Gobain Research Paris, 39 quai Lucien Lefranc, 93303 Aubervilliers, France*

Abstract

Stereocorrelation (SC) is a powerful tool for measuring 3D surface deformations in mechanical tests. However, it may suffer from convergence issues for large displacements or speckle changes. A global space-time formulation is proposed herein using Proper Generalized Decomposition (PGD) as a regularization strategy. The entire image sequence is considered as a whole, and the kinematics is sought as the sum of modes, each of which is a function of space multiplied by a function of time (smoothed over high frequencies if needed). A discriminative benchmark case is chosen to validate this approach: an impact test on glass laminated with PVB layers. This case is difficult for many reasons, particularly because of severe contrast changes due to light reflections occurring at several places. It is shown that the new formulation outperforms classical approaches in robustness and measurement accuracy and provides results within a much shorter processing time.

Keywords: Digital Image Correlation (DIC), High-speed camera, Impact test, Laminated glass, Proper Generalized Decomposition (PGD), Space-time regularization

1. Introduction

With the development of high-speed camera technology in the early 2000s, Digital Image Correlation (DIC) is becoming more and more popular to analyze dynamic tests by registering images of specimens at different time instants [1, 2, 3], because of its non-contact and non-destructive nature, as well as

*Corresponding author
Email address: xuyang.chang@ens-paris-saclay.fr (Xuyang Chang)
[1] Present address: Diamond Light Source, Harwell Science & Innovation Campus, Didcot, OX11 0DE, United Kingdom

full-field measurement capacity. The principle of DIC is to exploit the conservation of gray levels by minimizing, for instance, the quadratic differences between registered images. Among different variants, stereocorrelation (SC in the following, although 3D-DIC is often used in the literature) using two cameras [4, 5, 6] or more [7, 8] is extremely appealing since it grants access to 3D shapes and their deformations over regions of interest (ROIs) of external surfaces.

The first family of SC codes consists of independently registering multiple subsets, where the 3D kinematics and specimen shape are measured through local analyses and thus provide clouds of 3D points (each being the center of interrogation windows) [9, 10, 11, 4]. It is now referred to as *subset-based* or *local* SC [6, 5]. The second family, namely, *global* SC uses NURBS patches [12, 13] or Finite Element meshes [14, 15, 16] to describe the shape and kinematics of surfaces of interest. This approach offers a natural flexibility and compatibility to bridge the gap between experimental campaigns and numerical simulation tools (*e.g.,* Finite Element (FE) or isogeometric codes [17, 18]), since the same spatial discretization may be used for both simulation and experimental measurements. The latter (FE) approach is considered hereafter.

The intrinsic ill-posedness and its computational cost remain two major bottlenecks for SC codes. Experimental time series tend to be longer with the progress of imaging devices, particularly for high-speed tests, while each image has ever larger definitions. Hence, the large processing time of SC, which used to be affordable, may become limiting or at least demanding. Any algorithmic reformulation that reduces the computation load is thus more than welcome.

Inspired by the so-called Proper Generalized Decomposition (PGD) framework in the field of computational mechanics [19, 20, 21, 22], PGD-SC was pioneered by Passieux et al. [23] to circumvent the aforementioned computational cost issues. The idea was to approximate the sought displacement field as the sum of "modes", each of which was "separated" (*i.e.,* product of spatial fields and temporal functions). However, only one spatiotemporal mode was considered by the authors. Alternatively, the computation of the sought kinematics can be progressively updated with the best low-rank space-time approximations [24]. By uncoupling the space and time problems, the PGD approach significantly speeds up (stereo)correlation computations, and non-intrusive frameworks were devised [25, 23, 26]. Moreover, if required to circumvent the underlying ill-posedness, both temporal and spatial regularization can be easily implemented in these schemes [25, 24, 27].

The ill-posedness of FE-SC may appear from the over-abundant number of degrees of freedom [14, 15]. In such a case, the optimization, which lies at the heart of DIC and SC, leads to ill-conditioned Hessian matrices for Gauss-Newton schemes. To further improve the conditioning, Tikhonov regularization techniques or *a priori* assumptions may be added [7, 14, 28, 29]. However, it was reported that some types of spatial regularization also led to artifacts for kinematic measurements, for example, when large rotations occurred [26]. Alterna-

tively, spatial regularization[2] may also be implemented using modal approaches. Modal approaches were introduced to measure shape corrections [30], where the condition number of the modal Hessian matrix was significantly lowered compared to unregularized schemes. In the same spirit, such type of regularization can be equally introduced to perform deformation measurements.

In this paper, it is proposed to incorporate spacetime regularization, using the PGD framework, into FE-based SC. The different steps associated with standard and PGD-SC algorithms are discussed in Section 2, namely, calibration, global spatiotemporal SC formulation, the inclusion of spatial symmetry, spatial regularization, PGD framework, and temporal regularization. To challenge the proposed methodology, a difficult experimental case was chosen. Challenges associated with high-speed impact tests on laminated glass include large deformations, severe contrast changes due to specular light reflection, and long time series. The experimental configuration of the test is first introduced in Section 3. Then, Section 4 presents the relative performance of PGD-SC and a more classical (global in space, but local in time) SC analysis.

2. PGD Stereocorrelation

This section briefly recalls the main aspects of FE-based stereocorrelation (referred herein to as standard SC), and its extension to PGD stereocorrelation (PGD-SC) with possible space-time regularization. The interested reader may refer to Refs. [31, 7, 16] for additional details.

2.1. Construction of the 3D reference shape

For the sake of generality, SC is introduced with an arbitrary number $N_c \geq 2$ of cameras. The projection matrix $[\mathbf{\Pi}^m]$ for each camera, which is labeled $1 \leq m \leq N_c$, is required to relate the 4 homogeneous coordinates of 3D points $\{\mathbf{X}\}$ on the specimen surface with the 3 (homogeneous) coordinates of 2D projections $\{\mathbf{x}^m\}$ in each camera plane [4]

$$s^m\{\mathbf{x}^m\} = [\mathbf{\Pi}^m]\{\mathbf{X}\} \tag{1}$$

where s^m is the local scale factor.

In contrast with the most common choice of using one master camera and one slave [4], it is chosen to follow another route [12] where the observed surface is the 3D "master," and all cameras are related to the corresponding frame. If the 3D shape is well known, its surface pattern $\widehat{f}(\mathbf{X})$ (*i.e.,* gray level of speckle marking) can be constructed. With proper calibration, this unique reference pattern is estimated inside the region of interest common to all cameras as the average of images registered on the surface [7]

$$\widehat{f}(\mathbf{X}) = \frac{1}{N_c}\sum_{m=1}^{N_c} f^m(\mathbf{x}^m(\{\mathbf{X}\},[\mathbf{\Pi}^m]),t_0) \tag{2}$$

[2]Other variants of a prior spatial regularization exist, for instance, using B-splines or NURBS [7, 27].

where t_0 is the instant when a set of N_c images, f^m, of the sample in its reference state was acquired. Let us emphasize that accurate and reliable calibration is crucial for SC purposes to achieve robust 3D kinematic measurements and shape characterization [4, 32]. In the following, it is assumed that the calibration was performed successfully.

2.2. FE-based stereocorrelation

Among all different variants of stereocorrelation algorithms, the FE-based formulation consists in measuring the displacement field $\mathbf{U}(\mathbf{X},t)$ between reference and deformed images when minimizing the global residual for all N_c cameras at time t. For any trial displacement field $\mathbf{V}(\mathbf{X},t)$, the corrected image for the m-th camera, $\widetilde{f}^m_{\mathbf{V}}(\mathbf{x}^m(\{\mathbf{X}\},[\mathbf{\Pi}^m]),t)$ reads

$$\widetilde{f}^m_{\mathbf{V}}(\mathbf{x}^m(\{\mathbf{X}\},[\mathbf{\Pi}^m]),t) = f^m(\mathbf{x}^m(\{\mathbf{X}\}+\{\mathbf{V}(\mathbf{X},t)\},[\mathbf{\Pi}^m]),t) \tag{3}$$

where $f^m(\mathbf{x}^m,t)$ is the image acquired by the m-th camera at time t. From the previous setting, the local gray level residual $\rho^m_{\mathbf{V}}(\mathbf{X},t)$ is defined as

$$\rho^m_{\mathbf{V}}(\mathbf{X},t) = \rho^m_{\mathbf{V}}(\mathbf{x}^m(\{\mathbf{X}\},[\mathbf{\Pi}^m]),t) = \widehat{f}(\mathbf{X}) - \widetilde{f}^m_{\mathbf{V}}(\mathbf{x}^m(\{\mathbf{X}\},[\mathbf{\Pi}^m]),t) \tag{4}$$

The sought displacement field has to minimize the cost function written over the considered ROI

$$\mathbf{U}(\mathbf{X},t) = \underset{\mathbf{V}}{\operatorname{argmin}} \sum_{m=1}^{N_c} \|\rho^m_{\mathbf{V}}(\mathbf{x}^m,t)\|^2_{\mathrm{ROI}} \tag{5}$$

When an FE-based parameterization is assumed, the sought displacement field is written as

$$\mathbf{U}(\mathbf{X},t) = \sum_{i=1}^{N_x} a_i(t)\mathbf{\Phi}_i(\mathbf{X}) \tag{6}$$

where N_x is the number degrees of freedom (*i.e.,* the nodal displacements a_i), and $\mathbf{\Phi}_i(\mathbf{X})$ the corresponding (spatial) shape functions. The nodal amplitudes are gathered in the column vector $\{\mathbf{a}(t)\}$, which becomes the unknown to be determined at each time t via *instantaneous* registrations.

2.2.1. Instantaneous registration

Instantaneous registration consists in solving Equation (5) via Gauss-Newton iterations leading to linear systems written in terms of corrections $\{\delta\mathbf{a}(t)\}$ of nodal displacements

$$[\mathbf{H}_{\mathrm{inst}}]\{\delta\mathbf{a}(t)\} = \{\mathbf{B}_{\mathrm{inst}}(t)\} \tag{7}$$

with $[\mathbf{H}_{\mathrm{inst}}]$ the instantaneous Hessian matrix.

$$(\mathrm{H}_{\mathrm{inst}})_{ik} = \sum_{m}^{N_c} \int_{\mathrm{ROI}} (\mathbf{\Phi}_i \cdot \boldsymbol{\nabla}\widehat{f}(\mathbf{X}))^{\top} (\mathbf{\Phi}_k \cdot \boldsymbol{\nabla}\widehat{f}(\mathbf{X})) d\mathbf{X} \tag{8}$$

where $\boldsymbol{\Phi}_i$ represents the set of spatial shape functions, $\nabla\widehat{f}(\mathbf{X})$ represents the gradient of the intrinsic texture over the 3D model $\mathbf{X}$.

and $\{\mathbf{B}_{\text{inst}}(t)\}$ the right hand side term

$$(\mathrm{B}_{\text{inst}}(t))_i = \sum_m^{N_c} \int_{\text{ROI}} (\boldsymbol{\Phi}_i \cdot \boldsymbol{\nabla}\widehat{f}(\mathbf{X}))\rho_{\mathbf{V}}^m(\mathbf{x}^m, t)d\mathbf{X} \tag{9}$$

so that the total displacement $\mathbf{U}^n(\mathbf{X}, t)$ is updated with the incremental nodal displacement correction $\delta\mathbf{U}^n(\mathbf{X}, t) = \delta a_i(t)\boldsymbol{\Phi}_i(\mathbf{X})$

$$\mathbf{U}^{n+1}(\mathbf{X}, t) = \mathbf{U}^n(\mathbf{X}, t) + \delta\mathbf{U}^n(\mathbf{X}, t) \tag{10}$$

The local (*i.e.,* for each integration point) and global instantaneous residuals are conveniently normalized as

$$\begin{aligned}\rho_m(\mathbf{X}, t) &= \frac{\widehat{f}(\mathbf{X}) - \widetilde{f}_{\mathbf{U}}^m(\mathbf{x}^m(\{\mathbf{X}\}, [\boldsymbol{\Pi}^m]), t)}{\text{dyn}(\widehat{f}(\mathbf{X}))} \\ \rho_{\text{inst}}(t) &= \sqrt{\frac{1}{N_c}\sum^{m=N_c} \langle\rho_m(\mathbf{X}, t)^2\rangle_{\mathbf{X}}}\end{aligned} \tag{11}$$

where $\rho_m(\mathbf{X}, t)$ is the normalized local residual for the m-th camera, $\langle\cdot\rangle$ denotes the arithmetic average, and $\text{dyn}(\widehat{f}(\mathbf{X}))$ the dynamic range for the intrinsic texture.

The standard SC convergence criterion is evaluated through the stationarity of global instantaneous residual,

$$c_v = \frac{||\delta\rho_{\text{inst}}^n||}{||\rho_{\text{inst}}^n||} < 10^{-5} \tag{12}$$

Algorithm 1 summarizes the various steps of instantaneous SC when $t \leq t_f$, where t_f denotes the acquisition time of the last frame.

Algorithm 1 Instantaneous stereocorrelation

```
Initialize displacement field U                          ▷ Initialization
Compute instantaneous Hessian matrix, Eq. (8)
while t ≤ t_f do
    while Stationarity of ρ_inst(t) not reached, Eq. (12) do
        Update right-hand member {B_inst(t)}, Eq. (9)
        Compute incremental displacement correction {δa(t)}, Eq. (7)
        Update instantaneous displacement U, Eq. (10)
        Update instantaneous residuals ρ_U(x^m({X}, [Π^m]), t), Eq. (4)
    end while
    t ← t + 1,
    U(X, t) ← U(X, t − 1)        ▷ Use previous displacement as initialization
end while
```

2.2.2. Spatial regularization

Spatial regularization is a way of introducing additional prior information to reduce the effective number of degrees of freedom [6]. For the considered test-case discussed in the following sections, the expected displacement field was assumed to be axisymmetric (at least during the early stages of projectile impact). Hence, the displacement field only depended on the radial coordinate r instead of the full 2D coordinates, and the orthoradial displacement vanished. However, initially, an FE-mesh was designed over the region of interest, and it did *not* obey any particular symmetry. Therefore, the initial discretization including all degrees of freedom from the FE mesh was first chosen, from which the instantaneous Hessian matrix $[\mathbf{H}_{\text{inst}}]$ and second member $\{\mathbf{B}_{\text{inst}}\}$ were computed.

The axisymmetric regularization was implemented in a non-intrusive manner (*i.e.,* still using the initial mesh). The reduced basis $\breve{\mathbf{\Phi}}$ was projected onto the initial shape functions

$$\breve{\mathbf{\Phi}}_i(\mathbf{X}) = \sum_j S_{ij} \mathbf{\Phi}_j(\mathbf{X}) \tag{13}$$

Figures 1 and 2 show an example of an axisymmetric basis constructed with a mesh that was not axisymmetric. The reduction in degrees of freedom implies that the matrix $[\mathbf{S}]$ is rectangular. The problem (as well as the algorithm to solve it) remains the same, but with a modified Hessian matrix and right-hand vector. The spatial Hessian is reduced to a smaller matrix

$$[\mathbf{H}^{\text{axi}}_{\text{inst}}] = [\mathbf{S}][\mathbf{H}_{\text{inst}}][\mathbf{S}]^\top \tag{14}$$

while the second member becomes

$$\{\mathbf{B}^{\text{axi}}_{\text{inst}}\} = [\mathbf{S}]\{\mathbf{B}_{\text{inst}}\} \tag{15}$$

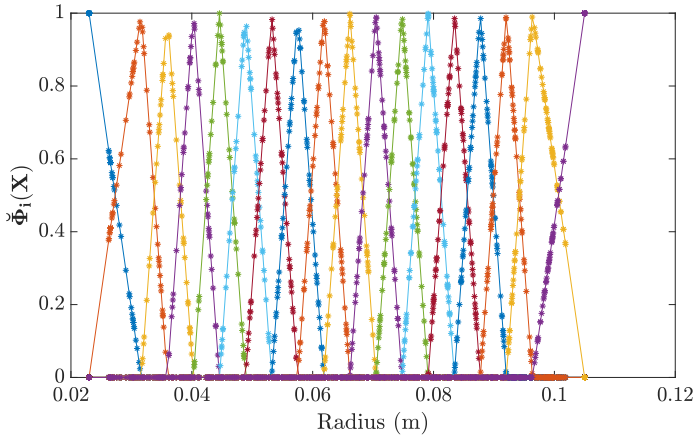

Figure 1: FE nodal coordinates projected onto an axisymmetric spatial discretization with a reduced number of degrees of freedom, $N_{\text{dof}} = 2 \times 18 = 36$

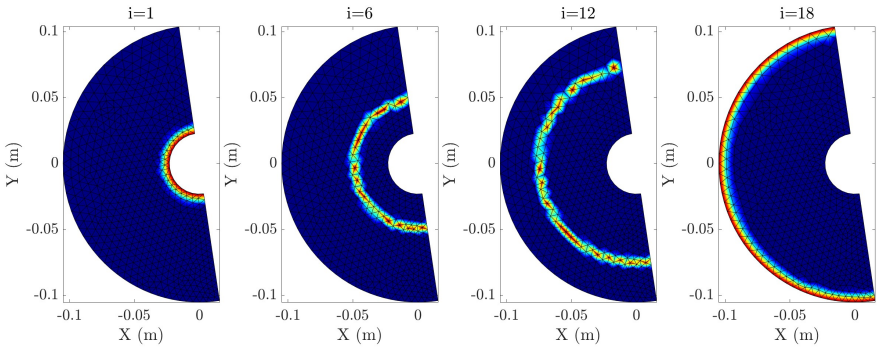

Figure 2: Axisymmetric mode $\breve{\mathbf{\Phi}}_\mathbf{i}(\mathbf{X})$ projected onto the chosen finite element mesh $i = 1, 6, 12, 18$

To account for smooth and regular deflections, low-pass spatial (radial) filters were applied to the instantaneous axisymmetric Hessian matrix, in order to penalize irregular radial displacement fluctuations

$$[\overline{\mathbf{H}}^{\text{axi}}_{\text{inst}}] = [\mathbf{H}^{\text{axi}}_{\text{inst}}] + p_1 \ell_1^2 [\mathbf{D_1}] + p_2 \ell_2^4 [\mathbf{D_2}] \tag{16}$$

where $[\mathbf{D_1}]$ and $[\mathbf{D_2}]$ penalize respectively the high frequency fluctuations of the first and second order radial derivatives of $\mathbf{U}$, p_1 and p_2 are the corresponding normalization coefficients, ℓ_1 and ℓ_2 the spatial regularization lengths.

In order to determine the appropriate normalization (p_1, p_2) for spatial regularization, a reference displacement field $\mathbf{T}$ is chosen, which contains a single characteristic length scale, λ, namely a sinusoidal waveform is a convenient example $\mathbf{T} = \sin\left(\dfrac{2\pi r}{\lambda}\right)\mathbf{e}_r$. The normalization coefficients are chosen such that the "energetic contribution" of each term in Equation (16) is equal

$$p_1 = \lambda^{-2}\frac{\{\mathbf{T}\}^\top[\mathbf{H}^{\text{axi}}_{\text{inst}}]\{\mathbf{T}\}}{\{\mathbf{T}\}^\top[\mathbf{D_1}]\{\mathbf{T}\}} \qquad p_2 = \lambda^{-4}\frac{\{\mathbf{T}\}^\top[\mathbf{H}^{\text{axi}}_{\text{inst}}]\{\mathbf{T}\}}{\{\mathbf{T}\}^\top[\mathbf{D_2}]\{\mathbf{T}\}} \tag{17}$$

2.3. Space-time stereocorrelation

Displacement fields are generally expected to be smooth in time. Hence, considering the SC objectives over the entire time sequence, one may exploit this time regularity to reduce the number of degrees of freedom with no prejudice to the ability of SC to capture the kinematic field, but with the benefit of better conditioning (*i.e.,* less prone to noise). Along the same spirit as spatial shape functions, $\mathbf{\Phi}_i(\mathbf{X})$, the time interpolation is proposed to be accounted for by a set of (a priori chosen) temporal shape functions, $\psi_j(t)$. Therefore, the

displacement field in space and time is written as

$$\mathbf{U}(\mathbf{X},t) = \sum_{i=1}^{N_x}\sum_{j=1}^{N_t} \alpha_{ij}\mathbf{\Phi}_i(\mathbf{X})\psi_j(t) \tag{18}$$

where N_x and N_t stand respectively for the number of degrees of freedom in space and time domains, α_{ij} the space-time amplitudes to be determined. They are obtained as a natural extension of the instantaneous SC formulation

$$\mathbf{U}(\mathbf{X},t) = \underset{\mathbf{v}}{\operatorname{argmin}} \ \|\rho(\mathbf{v})\|^2 = \underset{\mathbf{v}}{\operatorname{argmin}} \sum_{m=1}^{N_c} \left\| \widehat{f}(\mathbf{X}) - \widetilde{f}^m_{\mathbf{v}}(\mathbf{x}(\mathbf{X},\mathbf{\Pi}^m),t) \right\|^2_{\mathrm{ROI}\times[t_0;t_f]} \tag{19}$$

where $t \in [t_0;t_f]$ defines the time interval where the series of images has been acquired.

Similarly to Equation (8), the sought kinematics is progressively updated using an iterative Gauss-Newton scheme

$$[\mathbf{H}_{\mathrm{st}}]\{\delta\boldsymbol{\alpha}^n\} = [\mathbf{B}_{\mathrm{st}}] \tag{20}$$

$$\begin{array}{rcl} \delta\mathbf{U}^n(\mathbf{X},t) & = & \delta\alpha_{ij}\mathbf{\Phi}_i(\mathbf{X})\psi_j(t) \\ \mathbf{U}^{n+1}(\mathbf{X},t) & = & \mathbf{U}^n(\mathbf{X},t) + \delta\mathbf{U}^n(\mathbf{X},t) \end{array} \tag{21}$$

where the space-time Hessian matrix $[\mathbf{H}_{\mathrm{st}}]$ and second member $\{\mathbf{B}_{\mathrm{st}}\}$ read

$$\begin{array}{rcl} (\mathrm{H}_{\mathrm{st}})_{ijkl} & = & (\mathrm{H}_{\mathrm{inst}})_{ik}\ \mathrm{K}_{jl} \\ (\mathrm{B}_{\mathrm{st}})_{ik} & = & \displaystyle\sum_{m}^{N_c} \int_{t=t_0}^{t_f} (\mathrm{B}_{\mathrm{inst}}(t))_i \psi_k(t)\ dt \end{array} \tag{22}$$

where space and time contributions are decoupled. The "temporal" Hessian matrix $[\mathbf{K}]$ reduces to

$$K_{jl} = \int_{t=t_0}^{t=t_f} \psi_j(t)\psi_l(t)\ dt \tag{23}$$

If the temporal shape functions are orthonormal, then $[\mathbf{K}]$ is the identity matrix, and hence each iteration of space-time computation consists in solving N_t linear systems *independently*, with the instantaneous (*i.e.,* spatial) Hessian matrix $[\mathbf{H}_{\mathrm{inst}}]$ [25].

2.4. Proper Generalized Decomposition SC (PGD-SC)

Up to now, the spatial shape functions were chosen a priori from available tools, such as finite element shape functions over a mesh, or to account for specific symmetries such as the above-discussed axisymmetric case. Similarly, temporal shape functions were essentially unrestricted, and hence intuition or prior knowledge were at play. A powerful technique to reduce the number of degrees of freedom in the description of the displacement field $\mathbf{U}(\mathbf{X},t)$, is to consider Principal Component Analysis (PCA) [33], aka Proper Orthogonal

Decomposition (POD) [34]. The latter seeks the best low-rank approximation of a given set of data. POD, consists in searching for N_m modes to describe $\mathbf{U}(\mathbf{X}, t)$ at best

$$\mathbf{U}(\mathbf{X}, t) \approx \sum_{i=1}^{N_m} \alpha_i \mathbf{\Phi}_i(\mathbf{X}) \Psi_i(t) \tag{24}$$

where the L2-norm of the difference between the original data set and its low-rank approximation is minimized. This strategy allows space $\mathbf{\Phi}_i$ and time Ψ_i *modes* to be computed as eigenvectors. This approach works remarkably well as a post-processing technique when the displacement field is known, but cannot work before the solution is known.

In a similar spirit, the same low-rank approximation can be sought for any problem that can be recast in variational form. In that case, the variational form comes as a substitute to the L2-norm and hence is ideally fitted to the problem at hand [19, 20, 21, 22]. This approach is called "Proper Generalized Decomposition" or PGD. In the present framework, the variational form is naturally available from the norm of the residuals. In terms of algorithm, the idea is often to utilize a "greedy" approach where a single mode (in space and time) is computed at each iteration to minimize the residual error. After having computed temporal and spatial modes, the residual of the corrected problem is updated before a new iteration is started.

Benefiting from the global formulation of stereocorrelation, the PGD stereocorrelation residuals are first computed. Because space and time are decoupled in the global Hessian, (Equation (22)), it can be shown that the PGD temporal modes for the kinematics are in fact identical to the POD temporal modes of the residuals. Thus, the first task consists in computing the spatiotemporal residuals, $\rho_u(\mathbf{X}, t)$, and in extracting their temporal modes

$$\rho_u(\mathbf{X}, t) \approx \sum_{i}^{N_p} e_i \ \widehat{\chi}_i(\mathbf{X}) \ \widehat{\psi}_i(t) \tag{25}$$

where $\widehat{\chi}_i(\mathbf{X})$ and $\widehat{\psi}_i(t)$ represent, respectively, the i-th space and temporal mode ranked by their eigenvalues e_i in descending order. Note that $\widehat{\chi}_i(\mathbf{X})$ and $\widehat{\psi}_i(t)$ are normalized to 1, and are orthogonal between each other. The number of modes, N_p, is chosen so that the "power" (L2 norm) of the remainder is less than a prescribed fraction, ϵ, reads as

$$\begin{aligned} E_{\text{acc}}(N_p) &= \frac{\sum_{i=1}^{N_p} e_i^2}{\sum_{i=1}^{N_t} e_i^2} \\ E_{\text{acc}}(N_p) &\geq 1 - \epsilon \end{aligned} \tag{26}$$

The accumulated energy, $E_{\text{acc}}(N_p)$, represents the combined first N_p POD modes energetic contribution.
In this way, a number of temporal modes is first computed. As they are orthonormal, they are chosen in the global space-time approach, thereby leading

to as many N_p independent SC problems (the memory load of each modal space-time problem is equivalent to an instantaneous one). For any mode k, the SC problem to solve assumes the following form

$$\begin{aligned}(\mathrm{H}_{\mathrm{inst}})_{ij}\{\widehat{\phi}^k(\mathbf{X})\} &= \sum_{m=1}^{N_c}\int_{\mathrm{ROI}}\int_{t=t_0}^{t_f}(\phi_i(\mathbf{X})\cdot\nabla\widehat{f}(\mathbf{X}))e_k\widehat{\psi}_k(t)^2\widehat{\chi}_j(\mathbf{X})\;d\mathbf{X}dt \\ &= \sum_{m=1}^{N_c}e_k\int_{\mathrm{ROI}}(\phi_i(\mathbf{X})\cdot\nabla\widehat{f}(\mathbf{X}))\widehat{\chi}_j(\mathbf{X})\;d\mathbf{X}\end{aligned} \tag{27}$$

Note that the spatial modes $\widehat{\phi}^k$ are orthogonal only through one specific metric, namely that given by the instantaneous Hessian matrix. The set of modes $(\widehat{\phi}^k(\mathbf{X}),\widehat{\psi}^k(t))$ constitutes the PGD-solution of the SC problem. Because the temporal dimension only involves an Euclidean scalar product, the problem can be addressed from a mere POD in time. When the basis is completed by the corresponding modes in space, it becomes a non-trivial (PGD) approach endowed with its relevant metric.

Similarly compared to Standard SC, the space-time residuals are conventionally normalized as

$$\rho_{\mathrm{global}} = \frac{1}{t_f - t_0 + 1}\sum_{t_0}^{t=t_f}\rho_{\mathrm{inst}}(t) \tag{28}$$

The PGD SC convergence criterion is evaluated through the stationarity of global residual

$$c_v = \frac{||\delta\rho^n_{\mathrm{global}}||}{||\rho^n_{\mathrm{global}}||} < 10^{-5} \tag{29}$$

Let us underline the benefits of the proposed method to construct the temporal basis. Instead of enforcing a series of prescribed temporal shape functions, the PGD approach computes the temporal basis on-the-fly and determines the "best" set of modes in the temporal domain at each iteration. Algorithm 2 summarizes the different steps of PGD-SC.

Algorithm 2 PGD stereocorrelation

Initialize space-time displacement field $\mathbf{U}$ ▷ Initialization
Compute instantaneous Hessian matrix, Eq. (8)
while Stationarity of residual ρ_{global} not reached, Eq. (29) **do**
  Update spacetime residual, Eq. (4)
  Update temporal modes from current residuals, Eq. (25)
  Update spacetime right-hand member, Eq. (22)
  Compute incremental spacetime displacement correction, Eq. (27)
  Update space-time displacement, $\mathbf{U}(\mathbf{X},t) \leftarrow \mathbf{U}(\mathbf{X},t) + \delta\mathbf{U}(\mathbf{X},t)$, Eq. (21)
end while

2.5. Temporal regularization

Similar to the temporal regularization introduced in 2D-DIC [24], a "soft" temporal regularization was included inside the PGD-SC algorithm, during the construction of temporal modes. It consists in introducing a low pass filter, from an additional term to add in the minimization that penalizes solutions that would be too irregular in time. To filter out high-frequency fluctuations from $\widehat{\psi}_i$, one may add an additional quadratic cost function to the L2-norm of the residual

$$\int_{t_0}^{t_f} \left(\frac{d\rho(t)}{dt} \right)^2 \, dt \tag{30}$$

The weight of this additional cost function allows one to tune the cross-over time scale, τ, of the filter. Introducing the discrete-time derivative in matrix form $[\boldsymbol{D}]$, regularized temporal modes are obtained from a generalized POD-like problem with a metric given by

$$\{\boldsymbol{\rho}\}^\top \left([\mathbf{I}] + \tau^2 [\mathbf{D}]^\top [\mathbf{D}] \right) \{\boldsymbol{\rho}\} \tag{31}$$

Thus, after changing $\{\boldsymbol{\rho}\}$ into $\{\boldsymbol{\rho'}\} = \left([\mathbf{I}] + \tau^2 [\mathbf{D}]^\top [\mathbf{D}] \right)^{1/2} \{\boldsymbol{\rho}\}$, the solution is still given by a mere POD of $\{\boldsymbol{\rho'}\}$ (additional details are given in Ref. [24]). This soft regularization allows the time scale τ to be adjusted at will with no side cost. Note that setting $\tau = 0$ allows the temporal regularization to be disabled.

3. Impact test on laminated glass

Laminated glass is a material of choice for glazing. Sandwiched configurations made of two or more glass plies interleaved by polymeric interlayers are widely used as windshields, windows, or large panels in buildings, providing good transparency, thermal and acoustic insulation, and UV reflection [35]. Laminated glass is designed to retain large glass fragments created during impact and therefore to ensure consumer safety. The engineered adhesion between polymer and glass allows for finite strain regimes of cracked plates [36, 37], during which delamination of the interlayer and its stretching may dissipate a large amount of impact energy. Many standardized tests, including different dynamic loading conditions, were designed to validate the performance of glazing. For instance, the ball-drop test (a normalized test in the building industry [38]) is designed to evaluate the anti-burglar resistance of a laminate to three successive falls of a 4 kg steel ball. However, these tests are not suitable to qualify and quantify finely the glazing behavior under impact, which is mandatory to predict the composite behavior after glass breakage, and more importantly the delamination and stretching that may occur at the newly formed free surface locations.

The experimental device developed by Nourry [39] mimics the same loading conditions as *EN 356* standard on a 300×300 mm^2 layered glass plate. A dual high-speed camera system was set up around the impacted plate to measure the time-resolved shape of the impacted laminate via SC. A test lasts for a few

tens of milliseconds. Two 140 mm steel rings clamp the plate on both sides. A compressed air system launches a projectile on an impactor initially at rest in the barrel of the *cannon*, whose end is a half-sphere. After an adjusted stroke rate, the impactor hits the center of the plate surface, which starts to bend, then cracks initiate and propagate under intense hoop and radial stresses. After the first cracks have initiated, interlayer stretching and polymer-glass delamination occur. During this phase, the deformation of the back surface made of glass was monitored by two high-speed Photron® SA-5 cameras set on each side of the cannon axis (Figure 3 and Table 1).

Table 1: DIC hardware parameters of the stereoscopic system

Cameras	Photron® SA-5
Definition	640×376 pixels
Color filter	none
Gray Levels rendering	8 bits
Lens	Nikon AF Nikkor 24mm f/2.8D
Aperture	f/11
Field of view	500 mm $\times$ 300 mm = 0.15 m^2
Image scale	40 mm / 56 px$\approx$ 0.7 mm/px (in the center)
Stereo-angle	right camera: 33°, left camera: 37°
Stand-off distance	between 70 and 80 cm
Image acquisition rate	30,000 fps
Patterning technique	B/W paints
Pattern feature size	in the range of 3 to 10 pixels

Each camera monitored the test at 30,000 Hz with a definition of 640×376 pixels. To deal with short exposure time, lighting was provided by two 400-W spotlights put above the cannon axis (Figure 3). It is worth noting that the stereo-angles were high in comparison to standard practice. This choice was motivated by the present setup that had various protections against glass fragments and for lighting purposes.

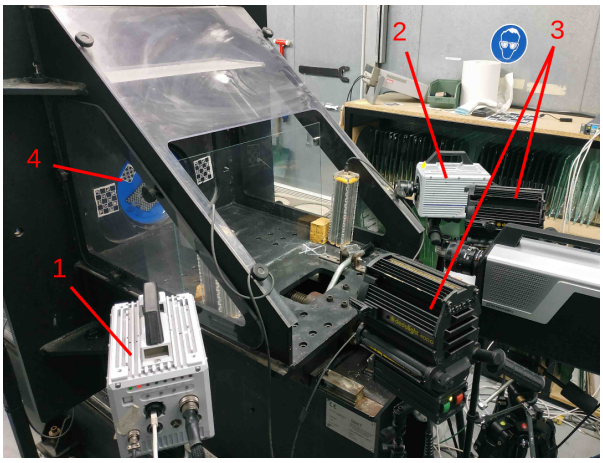

Figure 3: Stereovision set-up. 1- Left-side camera. 2- Right-side camera. 3- 400 W spotlights. 4- Laminated glass or, presently shown, the calibration dihedral through a 280 mm diameter circular window.

The speckle pattern was applied over half of the specimen surface, with the exception of a small central disk. The reason for painting such an ad-hoc region of interest is two-fold. First, the upper right half of glass remained untouched, allowing the evolution of the crack path and its pattern to be highlighted during the test. A white elastomeric (vinyl based) paint was deposited onto the semi-circular section of the observed surface. Black dots were sprayed over the surface to create a speckle pattern. This thin layer had good adhesion with glass and could be deformed into finite strain regimes before breakage. Therefore, the deformation of the laminate at late stages of glass ply fragmentation was accessible to SC analyses, which is a precious piece of information [40]. Second, the inner radius of the speckle pattern was very precisely prescribed and located at the center of the specimen so that it could be used as a trustworthy boundary to be used during the stereo-calibration procedure. To avoid potential obscuration related to poor camera perspective for large laminate deformation, an FE-mesh with a slightly reduced external radius was used. This central disk also helped to detect the small indentation that occurred during contact between the projectile and the plate, which could be used to validate the correct synchronization of the various cameras and sensors.

The full-field measurements of the glass surface were motivated by monitoring crack initiation and growth during the test, and by the 3D measurement of the deformed fragmented laminate to capture the extension of the PVB interlayer responsible for energy dissipation, and thereby to validate global models. Table 1 gathers all parameters that characterize the set-up, while Table 2 recalls the SC analysis parameters.

Table 2: Stereocorrelation analysis parameters

DIC software	Correli 3.0 [41]
Image filtering	None
Element sizes	1.5-1.7 mm ($\approx 25-26$ px, see Figure 2)
Shape functions	Linear (T3 elements)
Evaluation points (per element)	528 (*i.e.,* $N_{\mathrm{IP}} \approx 23$)
Matching criterion	Sum of squared differences (19)
Interpolant	Linear
Displacement noise-floor	≤ 40 µm

4. Proof of concept

In this section, the kinematics of laminated glass under projectile impact is analyzed. The details of stereo-calibration, axisymmetric formulation, spatial regularization and PGD implementations are discussed. The performance of PGD-SC and standard SC algorithms are compared.

4.1. Stereo-Calibration

The intrinsic calibration is primarily determined by referencing a calibration system (*i.e.,* an "open-book" calibration target decorated with several chessboards and CharUco markers). Then a self-calibration algorithm [12] is used to determine the extrinsic parameters, based on the random speckle pattern. As a final validation (Figure 4), the mesh was projected with the identified projection matrices and superimposed with the left and right raw images. A very accurate match was found between the painted speckle and projected mesh.

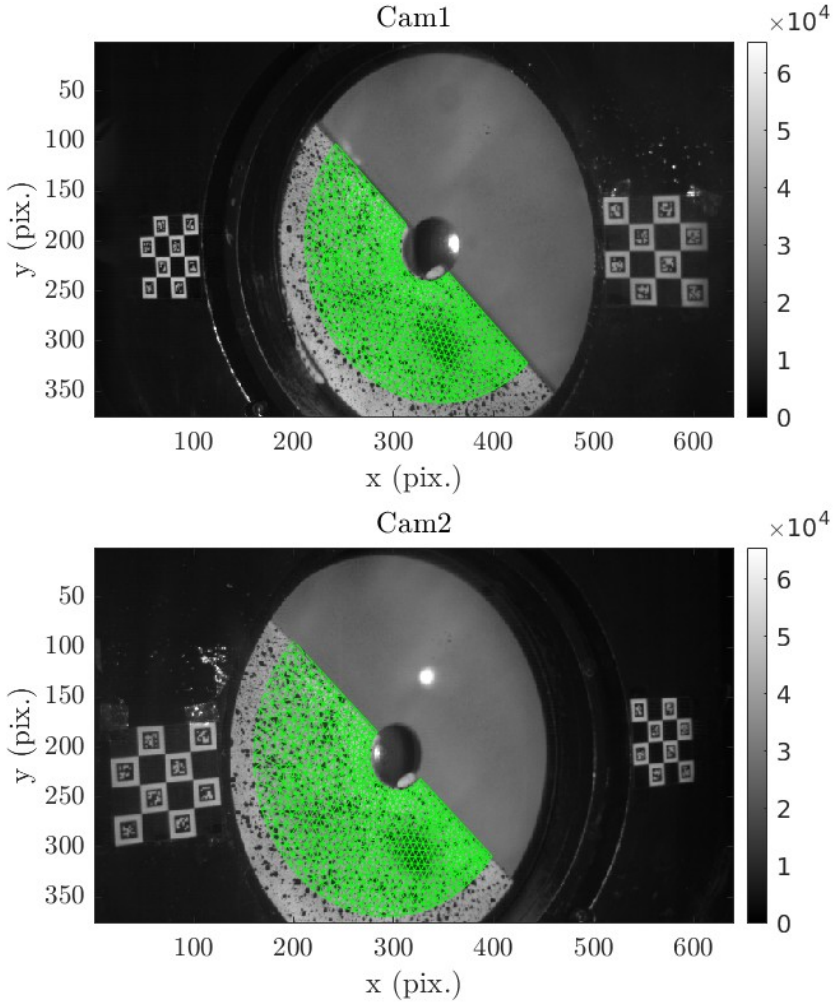

Figure 4: Projected mesh (in green) superimposed with raw images from cameras 1 and 2 (corresponding respectively to the left and right cameras of the set-up, after stereo-calibration.

4.2. Qualitative observations

In the following, the index t refers to the frame number in the image sequence. The corresponding time in seconds is $t/30000$ and the initial impactor speed is about 7.53 m/s. By plotting stereo-image sequences at different instants of time (Figures A.16 and A.17), several qualitative observations are made:

1. Before $t = 50$, the projectile has not yet reached the glass surface. The reference image is thus chosen as that acquired when $t = 50$.
2. At $t = 70$, (0.67 ms after impact), radial cracks in glass are first observed.

3. At $t = 90$, (1.33 ms after impact) along with the densification of radial cracks, orthoradial cracks initiated.
4. Between $t = 110$ and $t = 130$, due to the large rotation of some glass fragments, specular reflections of lighting are observed leading to local brightness saturation (particularly for the first camera (Figure A.16).
5. Between $t = 130$ and $t = 150$, a densification of orthoradial cracks is observed.
6. Despite very large out-of-plane motions during projectile impact, thanks to the PVB layer, few detachments of small glass fragments took place before $t = 250$ (*i.e.,* 6.6 ms after impact). The first fragment detachment is observed when $t = 247$.
7. After $t = 250$, the assumption of axisymmetry is no longer valid due to the progressive localization of PVB tearing. The SC analysis was thus carried out in when $t \in [50 : 250]$.

4.3. PGD-SC analyses

4.3.1. Temporal modes

The temporal basis, as produced by the PGD computation, is shown hereafter. First, the gray-level space-time residual $\rho(\mathbf{X}, t)$ was computed and arranged in matrix form (pixel index in one direction, and time in the other one). Temporal modes were computed using a time-regularized metric with $\tau = 10$ frames. A "greedy" sampling approach was implemented, namely, for the first 5 iterations, only the first temporal mode was used to approximate the kinematics ($N_t = 1$). Afterward, based on the "energy" criterion (26), the first N_t temporal modes ranked in descending order of their eigenvalues (Equation (5)) were selected to allow for more degrees of freedom in the temporal domain. In the present case, $N_t = 4$ revealed sufficient to account for 97% of the residual quadratic norm (Figure 5).

Let us note that, at each iteration, the corrected deformed images were updated with the estimated kinematics from the previous calculation (Equation (3)). Hence, the gray level residuals and corresponding low-rank approximation were progressively updated until convergence.

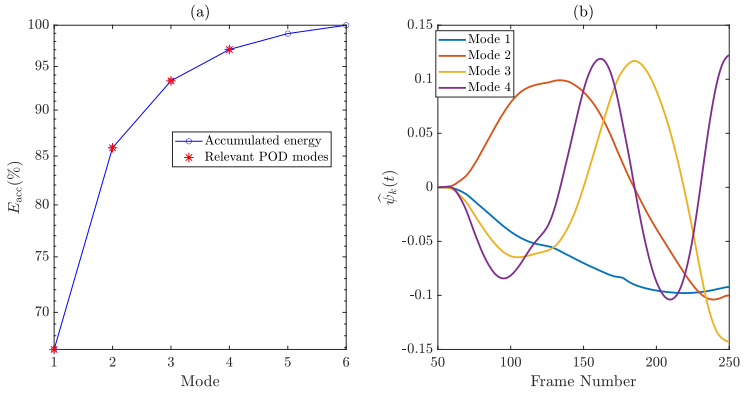

Figure 5: PGD temporal basis construction. (a) Accumulated energy contribution for the first 6 modes. The chosen number of modes, N_t, for PGD-SC (plotted with a red left cross) is determined so that more than 97% of the raw residual is accounted for. (b) First 4 temporal modes $\widehat{\psi}_k$ are plotted as a function of frame number

4.3.2. Temporal regularization

In order to highlight the impact of temporal regularization, the basis composed of the first four POD temporal modes were constructed with different frequency cut-offs, $\tau = 0$, 5, 10 and 20 frames (Figure 6).

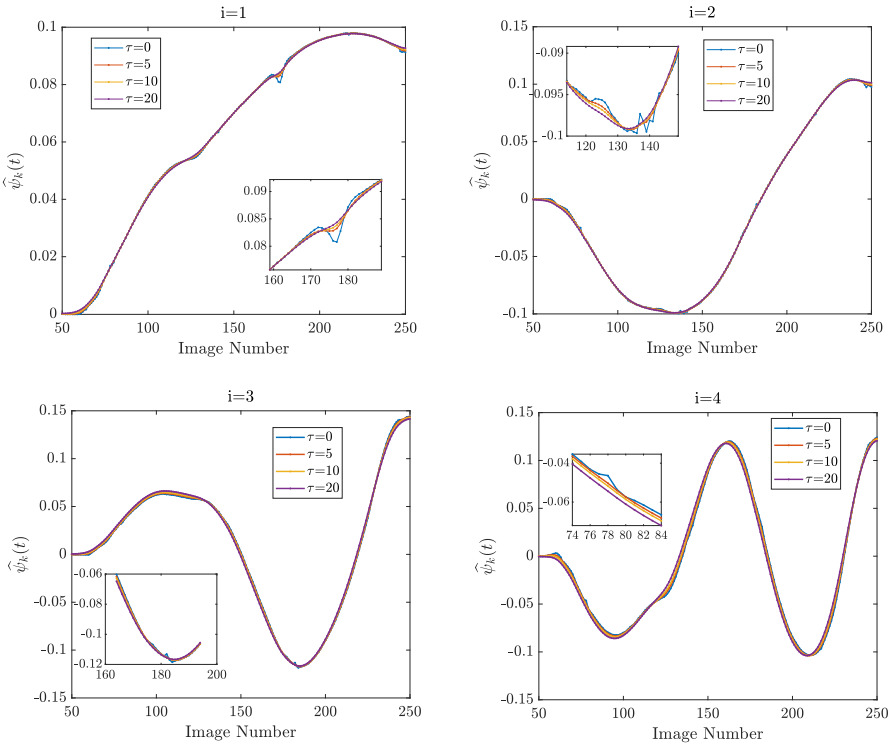

Figure 6: First i-th POD temporal modes constructed with different regularization durations

Several remarks are worth being made:

- With no temporal regularization (*i.e.,* $\tau = 0$), the first four temporal modes (with the highest energy contribution) were well estimated. However, the PGD temporal modes were prone to acquisition noise and abrupt gray-level variations.

- The major benefit of the regularization is highlighted in the first three or four modes when dealing with abrupt gray-level variation. As τ increases, the first four temporal modes were quite robust, but the sudden transition around $t \in [100, 140] \cup [160, 190]$ was significantly smoothed. The high-frequency oscillations were dampened; they were due to poor conditioning of the system, which made them very sensitive to model errors such as undesired specular reflections (very localized in space and time, as shown in Figure A.16), which caused brightness and contrast changes when the projectile and specimen were in contact. The temporal regularization with adequate regularization time $\tau = 10$ frames was an effective way of restoring the robustness of kinematic measurements and the choice of the"energy" criterion threshold became less user-dependent.

- Once PGD-SC had converged, a final refinement was performed by running one additional iteration with no temporal regularization. The change was modest but the result tolerated more rapid variations that were previously filtered. The fact that this last step was carried out after the main convergence ensured good stability (in contrast with using such a procedure from the start).

Last, the accumulated energy varies modestly when the regularization time increases (Figure 7).

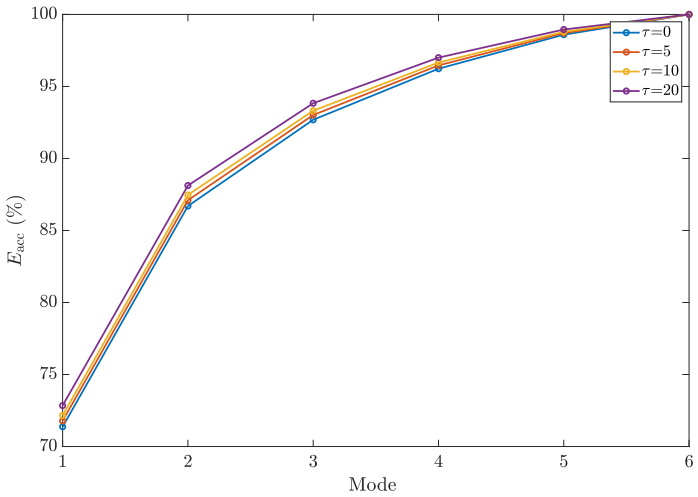

Figure 7: Accumulated energy constructed with different regularization durations

4.3.3. Convergence

The global and instantaneous residuals are plotted (for t sampled from 51 to 170) in Figure 8(a,b). A systematic decrease in iteration number is observed for all frames. The convergence is seen to be faster for the first frames, and occurs later for the last ones, which are more difficult to capture because of large displacements and specular reflections. Note that the instantaneous gray-level residuals decreased faster after 5 iterations as more temporal modes were taken into account.

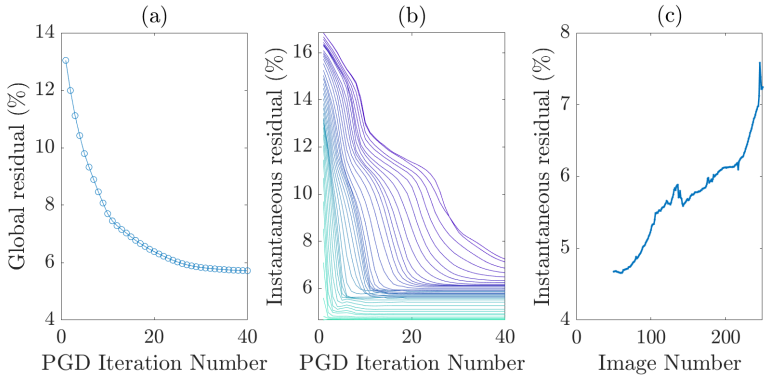

Figure 8: PGD residuals. (a) Global residual (over space and time) as a function of iteration number. (b) Change of residuals with iteration number for different frames sampled from $t = 51$ to $t = 250$ by steps of 10. The curve with the highest initial residual corresponds to the last deformed image ($t = 250$), while that with the lowest initial level corresponds to the first deformed image ($t = 51$). (c) Final instantaneous residual at convergence as a function of frame number.

After about 32 iterations, the residuals reached a stationary value. As shown in Figure 8(c), the final residual increased with the frame number (with a small bump between $t = 110$ and 130 due to the specular reflections). A closer inspection shows that this systematic increase has two origins (illustrations of some residual fields are proposed below). First, systematic brightness and contrast corrections would be needed to lower the difference between the reference image and the remainder of the sequence, and this change in gray levels due to progressive changes of orientation of the glass surface with respect to lighting (even ignoring specular reflection) matters. Second, the assumption of axisymmetry was sound in the early stages of the test, but became less valid as tearing of the PVB layer occurred preferentially along some cracks. Prior to this final stage $t \in [210, 250]$, fore-signs of this instability produced a breakdown of axisymmetry, initially progressive. Third, starting at $t = 247$, the detachment of a glass fragment moved into the region of interest for the first camera, thereby affecting the instantaneous residual very significantly, but after the fragment had flown away, the residual decreased again. The displacement field was mildly affected by this perturbation. Nonetheless, it was observed that these effects did not compromise the global convergence, as can be judged by the global residual computed over the entire sequence (Figure 8(a)).

4.4. Analysis of the Kinematics

4.4.1. Out-of-plane motions

With the measured displacement fields, deformed meshes were generated at each instant of time. Then, they were superimposed with the corresponding images, and colored according to the out-of-plane displacement amplitude. The choice of the unspeckled upper half of glass allows the presence of cracks to be

visually detected as well as local brightness-induced anomalies. In Figures 9 and 10, the displacement fields appear trustworthy since the deformed meshes, at different instants of time, match very accurately the edge of the speckled region in the deformed image sequence for both cameras, even when the displacement magnitude was quite high (*i.e.,* 35 mm). After $t = 250$, the first detached fragment flying over the region of interest (only in the first camera) is distinguished in Figure 9.

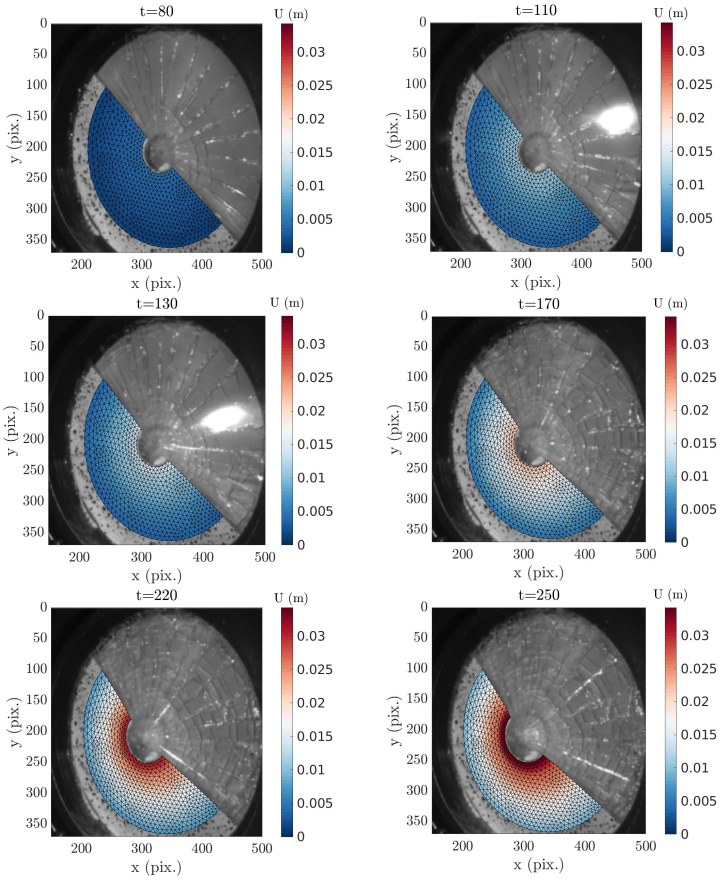

Figure 9: Out-of-plane motions superimposed with images acquired by the first stereo-camera at different instants of time $t = 80$, 110, 130, 170, 220 and 250

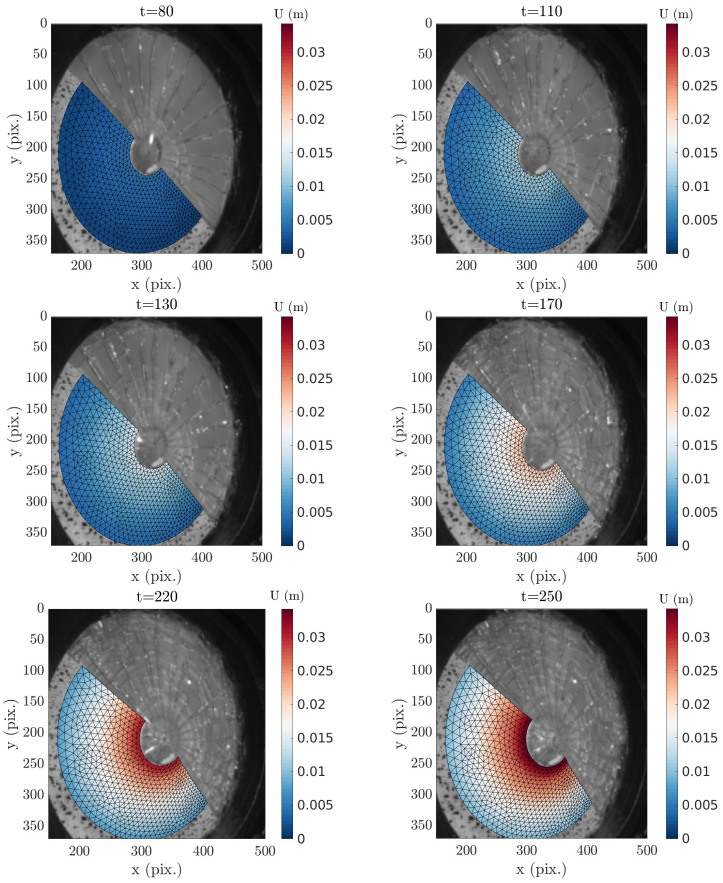

Figure 10: Out-of-plane motions superimposed with images acquired by the second stereo-camera at different instants of time $t = 80$, 110, 130, 170, 220 and 250

4.4.2. Residual fields

In this section, gray-level residual fields are displayed at several instants. Successively, intermediate (Figure 11) and late (Figure 12) frames will be discussed. Because of the axisymmetry of the displacement fields, it was possible to extrapolate the kinematics over the unspeckled region. Therefore, the gray-level residuals were computed accordingly over the *whole* specimen surface.

Brightness and contrast variations.
Along time, the gray level residuals appear to display different features that are not due to bad registration, but are rather interpreted as brightness and contrast (BC) variations (Figure 11).

- Geometry-related changes.
  Each camera captured the deformed geometry with a different orientation with respect to lighting. As a result, the gray level residuals of the first

camera were almost centered about zero, whereas, for the second camera, the upper part of the sample was brighter all along the deformation, where the bottom part was darker. Thus, the residuals appeared as positive or negative, respectively for the top and bottom regions. Such changes were gradual and explain most of the increase in the global residual that was reported earlier.

- Light reflection.
  As previously discussed and shown in Figure A.16, a very bright spot of specular reflection is seen with the first camera, and not at all with the second one (Figure A.17). Such type of observation is because only one camera was affected by this spurious reflection. With the axisymmetric spatial regularization (providing information at the same radius from the first camera), the PGD approach was not influenced too much by those highly localized residuals and could go through this time interval with a slight increase in the overall levels but still achieved reliable displacement measurements. Needless to say that more local approaches in space and in time would not overcome this obstacle.

- Radial cracks.
  For the speckled part, the occurrence of radial cracks created new glass surfaces that also contributed to specular reflection (starting from $t = 200$). They were much more localized in space and time and therefore had only a minimal contribution to the global residuals. As a consequence, they had almost no influence on convergence and on the evaluation of displacements.
  For the unspeckled region, the residual field is directly linked to cracks and associated brightness and contrast variations. Despite significant brightness and contrast variations due specular reflections, the residual field highlighted the presence of radial and orthoradial cracks under favorable orientation conditions.

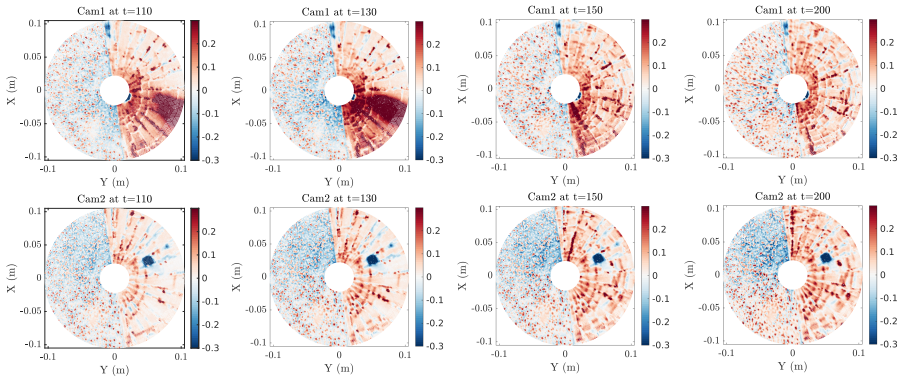

Figure 11: Dimensionless gray level residuals for cameras 1 (top) and 2 (bottom) when $t = 110$, 130, 150 and 200

Breakdown of axisymmetry.

For $t \in [240, 250]$ (Figure 12), the gray level residuals significantly increased as compared to the previous frames. In the speckled part, the top-down brightness changes in camera 2 were naturally more pronounced with time and thus larger displacements but smoothly varied angularly. The most salient feature already perceptible at $t = 240$ was the breakdown of axisymmetry, a basic assumption in the present analysis. In the very final stages of the test, stretching the PVB film induced a softening behavior that led to a gradual selection of fewer but more active cracks (with larger openings), while other minor cracks were shielded by the larger ones. This phenomenon developed progressively but ultimately led to the final tearing out of the PVB layer, which broke the axisymmetry. Moreover, for the first camera, the residuals were also higher close to the specimen center due to a larger motion and the aforementioned detached glass fragment but remained homogeneously distributed close to the clamping. The sudden separation between low and high residual along the orthoradial direction corresponds to the presence of multiple cracks that concentrate severe slope discontinuities, which are coupled with brightness changes.

In the unspeckled part, the residual fields from the first camera highlighted several major radial cracks (with large openings). From the second camera, the densification of orthoradial cracks confirmed the severe slope discontinuity observations from the speckled region.

These observations signal the limit of validity of the proposed approach. However, it is underlined that local SC would have failed much earlier than standard and, a fortiori, PGD approaches because of large out-of-plane motions and abrupt variations in gray-level due to cracks and significant geometry changes.

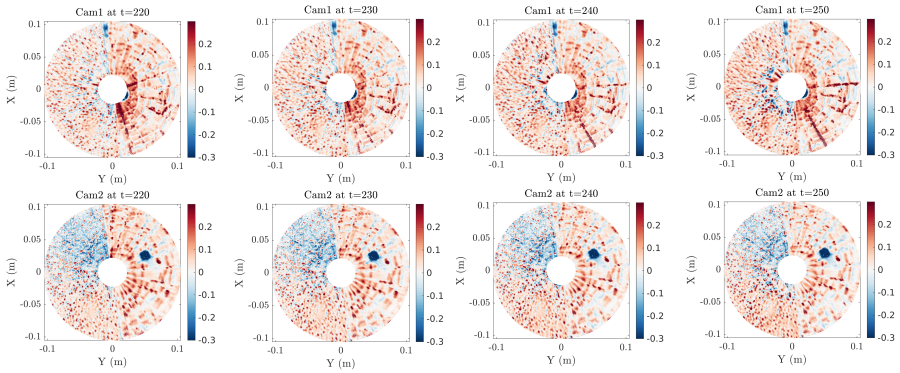

Figure 12: Dimensionless gray level residuals for cameras 1 (top) and 2 (bottom), at $t = 220$, 230, 240 and 250

4.5. Comparison of PGD-SC and standard SC

The performances of standard and PGD-SC are compared in this section. To allow for a fair comparison, the same FE-mesh, same axisymmetric regularization (i.e., same spatial regularization), same evaluation points, and same convergence criterion were used. The major difference was related to the temporal regularization. In standard SC, instantaneous calculations were carried out (*i.e.,* with no temporal regularization). Conversely, in PGD-SC, the temporal modes were regularized with $\tau = 10$ frames.

4.5.1. Measured Displacements

The measured displacement fields by both techniques are first compared. As shown in Figure 13, the measured kinematics was consistent between both approaches:
- concerning the out-of-plane component, both measurements coincided but for the last images of the sequence. When $t \approx 250$, none of the approaches was entirely satisfactory because of axisymmetry breakdown, which was prescribed in both approaches and the detachment of fragments (the gray-levels were no longer conserved for the first camera).
- the radial displacements measured by standard SC were significantly more fluctuating than those by PGD-SC (with a difference up to 0.8 mm).

This comparison shows that much more limited temporal degrees of freedom associated with the PGD formulation (4 modes vs. 200 frames) did not constrain too much the resolved displacements. The high-frequency components were effectively filtered out by temporal regularization implemented in PGD-SC.

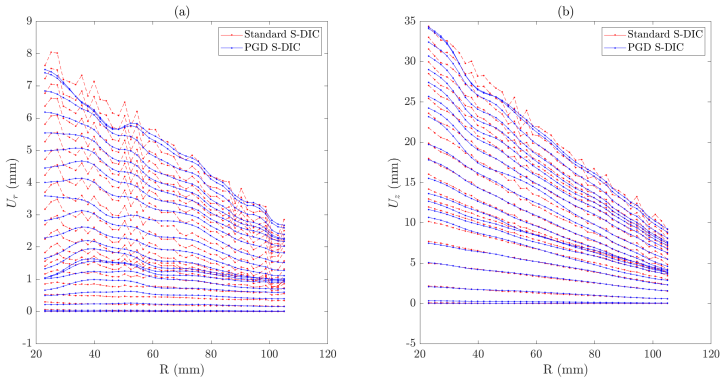

Figure 13: Comparison between measured nodal displacements for different frames with a step size of 10. The PGD-SC results are plotted as blue dots and standard SC measurements with red dots. Displacement amplitudes along the out-of-plane (a) and radial (b) directions.

4.5.2. Instantaneous residual

The instantaneous gray-level residuals obtained from PGD and standard SC (with spatial regularization applied in both analyses) are displayed in Figure 14. The residuals of both approaches nearly coincided at each instant of time, thereby validating PGD-SC for most of the sequence.

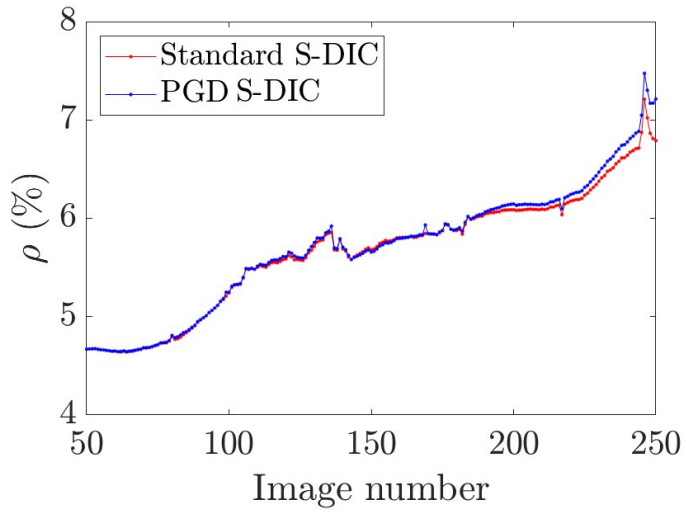

Figure 14: Instantaneous residual (PGD-SC residual plotted as red cross and standard SC with blue dots) for each analyzed frame

4.5.3. Computational Cost

The average iteration number per image was also compared as an indicator of the computational cost. As shown in Figure 15(a), the average iteration number per image for standard SC was 17.3, and it was shortened to 15.2 when using PGD-SC, which was a reduction of more than 13%. Moreover, the computation time of standard SC was 44% higher than that of PGD-SC (Figure 15(b)). Therefore, a significant improvement was achieved using PGD-SC instead of standard SC.

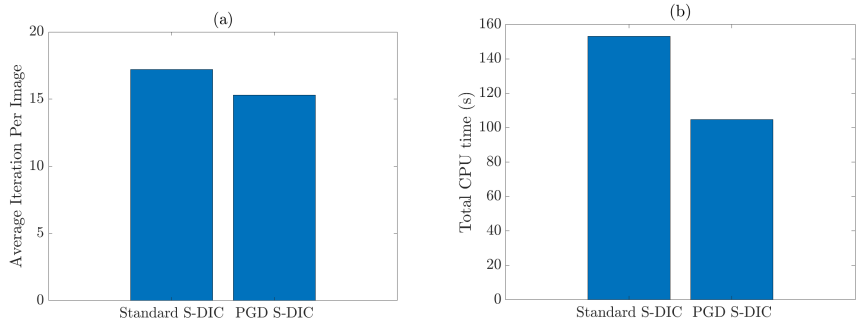

Figure 15: Comparison of average iteration number (a) and total CPU time (b) for both approaches

5. Conclusion

In this paper, a novel global stereocorrelation framework combining space-time regularization and PGD setting with multiple modes was presented. This framework addressed the major drawbacks of standard stereocorrelation analyses, namely, their ill-posedness and computational cost. In order to illustrate the methodology, a rather demanding test case was chosen, namely, a high-speed impact test on a PVB laminated glass sample. The large shape variations during impact and resulting light reflections induced significant gray-level changes that may compromise the capacity of classical stereocorrelation analyses to handle such situations.

The space-time regularization and the PGD variant were seamlessly integrated into an existing FE-SC code with minimal workload. The introduction of symmetry constraints was chosen for spatial regularization, which was implemented in a non-intrusive manner. It significantly reduced the number of spatial degrees of freedom, hence ensuring a much lower condition number. Similarly, high-frequency oscillations in temporal modes were induced from salient but artifactual specular reflections leading to brightness and contrast variations or acquisition noise and other acquisition anomalies. These "fragile" modes were stabilized using temporal regularization, which was an efficient way to mitigate high-frequency oscillations.

The performances of standard and PGD-stereocorrelation were compared in terms of measured displacement fields, gray-level residuals, and computation

cost. The measured displacements were very close as well as both residuals. With the same spatial regularization, the kinematic fields measured by PGD-SC were smoother than with standard SC (especially the radial displacement component). The run time was reduced by a factor of more than 44 % as compared to standard SC.

Last, let us emphasize that the separation of variables is not restricted to kinematic bases. Model parameters may be included as extra coordinates [21]. For instance, it is possible to incorporate brightness and contrast corrections into PGD-SC computations. Such implementation is underway and will be reported in future works.

Acknowledgments

The "cannon" experiment was made possible with different pieces of equipment provided by Saint-Gobain Research Compiègne, Saint-Gobain Research Paris and ENS Paris-Saclay, who are gratefully acknowledged. Many thanks to Quentin Guy de Chamisso, Grégorie Remeur and Richard Villey for conducting the cannon tests. We acknowledge useful suggestions and discussions with Xavier Brajer, René Gy and Keyvan Piroird. CLG was supported by the ANRT and Saint-Gobain Research Paris through a CIFRE grant.

Appendix A. Image sequence acquired by both cameras

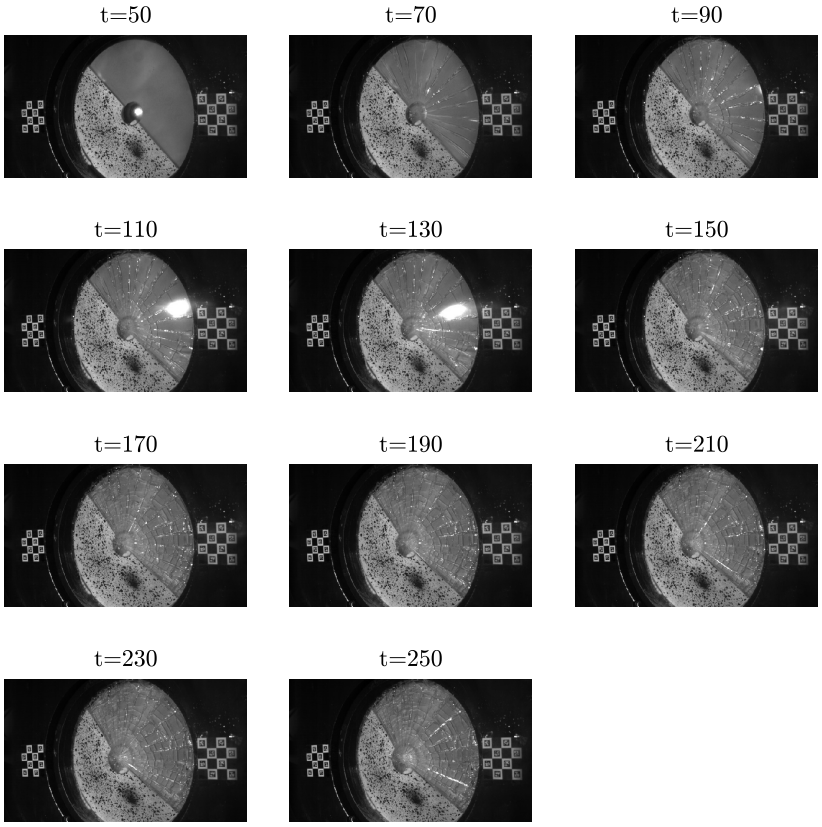

Figure A.16: Image sequence acquired by the first camera from $t = 50$ to 250

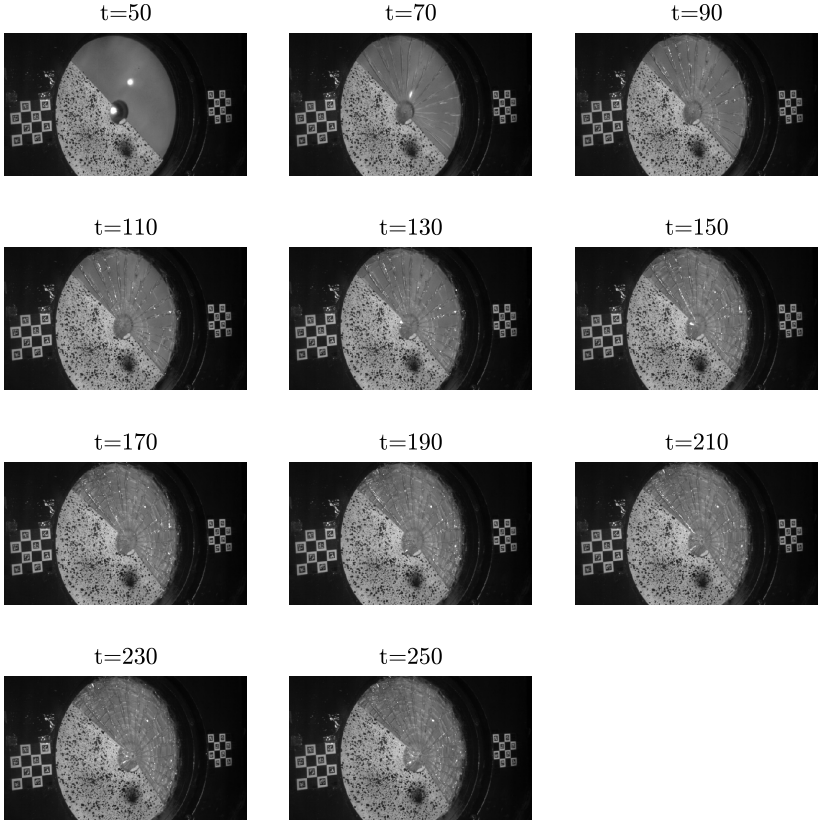

Figure A.17: Image sequence acquired by the second camera from $t = 50$ to 250

References

[1] Helfrick, M.N., Niezrecki, C., Avitabile, P., Schmidt, T.: 3D Digital image correlation methods for full-field vibration measurement. Mechanical Systems and Signal Processing **25**(3), 917–927 (2011). https://doi.org/10.1016/j.ymssp.2010.08.013

[2] Reu, P.L., Rohe, D.P., Jacobs, L.D.: Comparison of DIC and IDV for practical vibration and modal measurements. Mechanical Systems and Signal Processing **86**, 2–16 (2017). https://doi.org/10.1016/j.ymssp.2016.02.006.

[3] Hild, F., Bouterf, A., Roux, S.: Measurement of kinematic fields via DIC for impact engineering applications. International Journal of Impact Engineering **130**, 163–171 (2019) https://doi.org/10.1016/j.ijimpeng.2019.04.007

[4] Sutton, M.A., Orteu, J.J., Schreier, H.: Image Correlation for Shape, Motion and Deformation Measurements: Basic Concepts, Theory and Applications. Springer, New York, NY (USA) (2009) https://doi.org/10.1007/978-0-387-78747-3

[5] Sutton, M.A.: Computer vision-based, noncontacting deformation measurements in mechanics: A generational transformation. Applied Mechanics Reviews **65**(AMR-13-1009), 050802 (2013) https://doi.org/10.1115/1.4024984

[6] Hild, F., Roux, S.: Digital image correlation. In: Rastogi, P., Hack, E. (eds.) Optical Methods for Solid Mechanics. A Full-Field Approach, pp. 183–228. Wiley-VCH, Weinheim (Germany) (2012)

[7] Dufour, J.-E., Hild, F., Roux, S.: Shape, Displacement and Mechanical Properties from Isogeometric Multiview Stereocorrelation. Journal of Strain Analysis for Engineering Design **50**(7), 470–487 (2015) https://doi.org/10.1177/0309324715592530

[8] Wang, Y., Charbal, A., Dufour, J.-E., Hild, F., Roux, S., Vincent, L.: Hybrid multiview correlation for measuring and monitoring thermomechanical fatigue test. Experimental Mechanics (2019). https://doi.org/10.1007/s11340-019-00500-8

[9] Luo, P.F., Chao, Y.J., Sutton, M.A., Peters, W.H.: Accurate measurement of three-dimensional deformations in deformable and rigid bodies using computer vision. Experimental Mechanics **33**, 123–132 (1993) https://doi.org/10.1007/BF02322488

[10] Helm, J.D., McNeill, S.R., Sutton, M.A.: Improved three-dimensional image correlation for surface displacement measurement. Optical Engineering **35**(7), 1911–1920 (1996) https://doi.org/10.1117/1.600624

[11] Sutton, M.A., McNeill, S.R., Helm, J.D., Chao, Y.J.: Advances in two-dimensional and three-dimensional computer vision. In: Rastogi, P.K. (ed.) Photomechanics, vol. Topics in Appl. Phys., 77, pp. 323–372. Springer, Berlin (Germany) (2000)

[12] Beaubier, B., Dufour, J.E., Hild, F., Roux, S., Lavernhe-Taillard, S., Lavernhe-Taillard, K.: CAD-based calibration of a 3D-DIC system: Principle and application on test and industrial parts. Experimental Mechanics **54**(3), 329–341 (2014) https://doi.org/10.1007/s11340-013-9794-6

[13] Dufour, J.-E., Beaubier, B., Hild, F., Roux, S.: CAD-based displacement measurements. Principle and first validations. Experimental Mechanics **55**(9), 1657–1668 (2015) https://doi.org/10.1007/s11340-015-0065-6

[14] Dubreuil, L., Dufour, J.-E., Quinsat, Y., Hild, F.: Mesh-based shape measurements with stereocorrelation. Experimental Mechanics **56**(7), 1231–1242 (2016) https://doi.org/10.1007/s11340-016-0158-x

[15] Pierré, J.-E., Passieux, J.-C., Périé, J.-N.: Finite Element Stereo Digital Image Correlation: Framework and Mechanical Regularization. Experimental Mechanics **57**(3), 443–456 (2017) https://doi.org/10.1007/s11340-016-0246-y

[16] Berny, M., Archer, T., Beauchêne, P., Mavel, A., Hild, F.: Displacement Uncertainty Quantifications in T3-Stereocorrelation. Experimental Mechanics **61**, 771–790 (2021) https://doi.org/10.1007/s11340-021-00690-0

[17] Zienkievicz, O.C., Taylor, R.L.: The Finite Element Method. 4th edition. McGraw-Hill, London (UK) (1989)

[18] Cottrell, J.A., Hughes, T.J.R., Bazilevs, Y.: Isogeometric Analysis: Toward Integration of CAD and FEA. Wiley (2009) https://doi.org/{10.1002/9780470749081.ch7}

[19] Chinesta, F., Ladeveze, P., Cueto, E.: A short review on model order reduction based on proper generalized decomposition. Archives of Computational Methods in Engineering **18**(4), 395 (2011). https://doi.org/10.1007/s11831-011-9064-7

[20] Ladevèze, P.: Nonlinear Computational Structural Mechanics: New Approaches and Non-incremental Methods of Calculation. Springer (2012) https://doi.org/10.1007/978-1-4612-1432-8

[21] Chinesta, F., Leygue, A., Bordeu, F., Aguado, J.V., Cueto, E., Gonzalez, D., Alfaro, I., Ammar, A., Huerta, A.: Pgd-based computational vademecum for efficient design, optimization and control. Archives of Computational Methods in Engineering **20**(1), 31–59 (2013). https://doi.org/10.1007/s11831-013-9080-x

[22] Ladevèze, P.: PGD in linear and nonlinear computational solid mechanics. In: Separated Representations and PGD-Based Model Reduction, pp. 91–152. Springer (2014) https://link.springer.com/chapter/10.1007/978-3-7091-1794-1_3

[23] Passieux, J.-C., Bouclier, R., Périé, J.N.: A Space-Time PGD-DIC algorithm: Application to 3D mode shapes measurements. Experimental Mechanics **58**(7), 1195–1206 (2018). https://doi.org/10.1007/s11340-018-0387-2

[24] Berny, M., Jailin, C., Bouterf, A., Hild, F., Roux, S.: Mode-enhanced space-time DIC: applications to ultra-high-speed imaging. Measurement Science and Technology **29**(12), 125008 (2018) https://dx.doi.org/10.1088/1361-6501/aae3d5,

[25] Berny, M., Archer, T., Mavel, A., Beauchêne, P., Roux, S., Hild, F.: On the analysis of heat haze effects with spacetime DIC. Optics and Lasers in Engineering **40**, 544–556 (2018) https://doi.org/10.1016/j.optlaseng.2018.06.004

[26] Colantonio, G., Chapelier, M., Bouclier, R., Passieux, J.-C., Marenić, E.: Noninvasive multilevel geometric regularization of mesh-based three-dimensional shape measurement. International Journal for Numerical Methods in Engineering **121**(9), 1877–1897 (2020) https://doi.org/10.1002/nme.6291

[27] Chapelier, M., Bouclier, R., Passieux, J.-C.: Free-form deformation digital image correlation (ffd-dic): A non-invasive spline regularization for arbitrary finite element measurements. Computer Methods in Applied Mechanics and Engineering **384**, 113992 (2021). https://doi.org/10.1016/j.cma.2021.113992

[28] Pierré, J.-E., Passieux, J.-C., Périé, J.-N.: Finite Element Stereo digital image correlation: Framework and mechanical regularization. Experimental Mechanics **57**(3), 443–456 (2017). https://doi.org/10.1007/s11340-016-0246-y

[29] Wang, Y., Charbal, A., Dufour, J.E., Hild, F., Roux, S., Vincent, L.: Hybrid multiview correlation for measuring and monitoring thermomechanical fatigue test. Experimental Mechanics **60**(1), 13–33 (2020). https://doi.org/10.1007/s11340-019-00500-8

[30] Etievant, D., Quinsat, Y., Thiebaut, F., Hild, F.: A modal approach for shape defect measurement based on global stereocorrelation. Optics and Lasers in Engineering **128**, 106030 (2020). https://doi.org/10.1016/j.optlaseng.2020.106030

[31] Passieux, J.-C., Réthoré, J., Gravouil, A., Baietto, M.-C.: Local/global non-intrusive crack propagation simulation using a multigrid x-fem solver.

Computational Mechanics **52**(6), 1381–1393 (2013). https://doi.org/10.1007/s00466-013-0882-3

[32] Dufour, J.-E., Beaubier, B., Hild, F., Roux, S.: CAD-based displacement measurements with Stereo-DIC. Experimental Mechanics **55**(9), 1657–1668 (2015) https://doi.org/10.1007/s11340-015-0065-6

[33] Abdi, H., Williams, L.J.: Principal component analysis. WIREs Computational Statistics **2**(4), 433–459 (2010) https://doi.org/10.1002/wics.101

[34] Chatterjee, A.: An introduction to the proper orthogonal decomposition. Current Science **78**(7), 808–817 (2000) https://www.jstor.org/stable/24103957

[35] Martín, M., Centelles, X., Solé, A., Barreneche, C., Fernández, A.I., Cabeza, L.F.: Polymeric interlayer materials for laminated glass: A review. Construction and Building Materials **230**, 116897 (2020). https://doi.org/10.1016/j.conbuildmat.2019.116897

[36] Del Linz, P., Hooper, P.A., Arora, H., Wang, Y., Smith, D., Blackman, B.R.K., Dear, J.P.: Delamination properties of laminated glass windows subject to blast loading. International Journal of Impact Engineering **105**, 39–53 (2017). https://doi.org/10.1016/j.ijimpeng.2016.05.015.

[37] Elzière, P., Dalle-Ferrier, C., Barthel, E., Creton, C., Ciccotti, M.: Large strain viscoelastic dissipation during interfacial rupture in laminated glass. Soft Matter **13** (2017). https://doi.org/10.1039/C6SM02785G

[38] Norme Européenne: NF EN 356. Verre dans la construction – Vitrage de sécurité – Mise à l'essai et classification de la résistance à l'attaque manuelle (2000)

[39] Nourry, E.: Laminated glass behaviour under perforating impact. Thesis, Arts et Métiers ParisTech (March 2005). https://pastel.archives-ouvertes.fr/pastel-00001608

[40] Le Gourriérec, C.: Multi-instrumented dynamic experiments on laminated glass. . Thesis, Université Paris-Saclay (Dec 2022). http://www.theses.fr/2022UPAST166

[41] Leclerc, H., Neggers, J., Mathieu, F., Hild, F., Roux, S.: Correli 3.0. IDDN.FR.001.520008.000.S.P.2015.000.31500, Agence pour la Protection des Programmes, Paris (France) (2015)